Nearfield Summary and Analysis of the Third AIAA Sonic Boom Prediction Workshop C608 Low Boom Demonstrator

Michael A. Park* and Melissa B. Carter†
NASA Langley Research Center, Hampton, VA 23681, USA

A summary and statistical analysis of the nearfield Computational Fluid Dynamics (CFD) submissions for the Third AIAA Sonic Boom Prediction Workshop is provided with a focus on the C608 Low Boom Flight Test Demonstrator. The C608 is more complex in terms of geometry and propulsion boundary conditions than previous workshop cases and is more representative of vehicles with lower ground loudness and the potential for lower annoyance. The nearfield signatures submitted by the participants are propagated to the ground to compute statistics of loudness measures over the vehicle sonic boom carpet. Principle component analysis is used to extract the primary variation modes. Context from previous sonic boom workshops indicates that this workshop has the lowest variation even though the case is more challenging because it is quieter and more complex. The results documented in this summary indicate that the international state-of-the-art for nearfield CFD has a variation that is small enough for meaningful low-boom design and analysis. Low-boom configuration analysis methods with low variation are important tools to develop certification processes for addressing the prohibition on overland supersonic commercial flight.

Nomenclature

Δp	pressure difference from ambient (Pa)
$\Delta p/p_\infty$	Freestream pressure difference normalized by freestream
h	Characteristic spacing of the grid
N	Number of control volumes
PL	Perceived Level (dB)
X	Horizontal distance from the nose (inches)
Φ	Offtrack angle (zero is directly below model)

I. Introduction

The Third American Institute of Aeronautics and Astronautics (AIAA) Sonic Boom Prediction Workshop (SBPW3) was held on January 4–5, 2020 at Orlando, Florida. This workshop was a sequel to the First (SBPW1) and Second (SBPW2) Workshops as documented by Park and Morgenstern [1] and Park and Nemec [2]. The first day of SBPW3 featured analysis of the nearfield pressure field of a low boom flight demonstrator prototype and a shock-plume interaction wind tunnel model. The wind tunnel model submissions were summarized by Carter and Park [3]. The second day of the workshop focused on atmospheric propagation as detailed by Rallabhandi and Loubeau [4]. There were approximately 50 attendees. The objective of the first day of this workshop was to assess the state of the art for predicting nearfield pressure signatures needed for accurate and reliable sonic boom prediction. Nearfield pressure signatures, extracted from Computational Fluid Dynamics (CFD) solutions, were gathered from the international participants. The participants were required to use a series of uniformly-refined, workshop-provided meshes. Participants also created meshes with their best practices for computing nearfield pressure signatures on the provided geometries.

The submissions to this workshop indicated a number of clear trends as compared to previous sonic boom workshops. The number of adapted mesh solutions increased and there was an influx of participation by commercial CFD vendors.

*Research Scientist, Computational AeroSciences Branch, AIAA Associate Fellow.
†Aerospace Engineer, Configuration Aerodynamics Branch, AIAA Associate Fellow.

An axisymmetric case from SBPW2 was requested during the notice of intent to participate phase, which helped to improve the consistency of submissions to this workshop. Two nearfield CFD cases were required for SBPW3: the biconvex and C608. The required SBPW3 cases met and exceeded the complexity of optional cases from previous workshops.

SBPW3 focuses on nearfield CFD, but predicting the acoustic signature on the ground and how it is perceived by humans is the goal of the sonic boom community, see Fig. 1. The SBPW3 participants submitted nearfield pressure signatures. While these signatures could be compared directly to each other, propagating the nearfield signatures to the ground and reducing the properties of these signatures to loudness enables mesh-refinement studies and the application of statistical methods such as N-version testing [5]. The propagation and loudness calculations were performed by the authors, not by the participants, in an attempt to apply these methods as uniformly as possible to the submissions. The descriptive statistical products and mesh convergence studies continue the process of quantifying the variation of nearfield CFD employed by the international participants. SBPW3 benefits from the lessons learned at the 2008 NASA Sonic Boom Prediction Workshop [6], SBPW1 [1, 7], and SBPW2 [2, 8]. Experience from AIAA Drag [9, 10], High Lift [11], and Shock Boundary Layer Interaction [12] Prediction Workshops also contributed to the success of the current workshop.

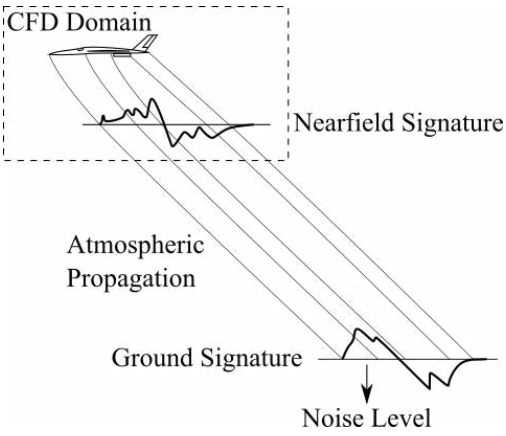

Fig. 1 Sonic boom prediction process.

A website (`lbpw.larc.nasa.gov`) was used to organize the workshop and disseminate results. This includes all the participant presentations, computational meshes, and submitted results to encourage continued research. Workshop participants also published details of their analysis in conference papers organized into an invited special session at the AIAA AVIATION 2020 conference in conjunction with this summary.

The data and analysis methods of this summary are intended to contribute toward the discussion of replacing the prohibition of overland supersonic flight [13] with a certification standard. The existing ban on overland flight increases the cost and block time of supersonic flights between city pairs [14] and is an important driver of the economic viability of a supersonic transport [15, 16].

II. C608 Description

The C608 is a modified preliminary design of the Lockheed Martin X-59 QueSST for NASA's Low-Boom Flight Demonstration mission, see Fig. 2. While the C608 is representative of a low-boom demonstrator vehicle, modifications made to the C608 geometry to facilitate release of the model to the SBPW3 participants prevent direct comparison of the results to the X-59 configuration. Technology for the C608 has origins in the Lockheed Martin contribution to the NASA N+2 supersonic airliner concept design studies [17–19].

The geometry and meshes are provided in the correct incidence for simulation at 0° angle of attack by including a rotation about the nose of 2.15° to include the design incidence. Control surfaces are positioned for a representative cruise condition. To permit release to the international workshop community, the nozzle inner mold line has been replaced with a generic example from Putnam and Capone [20] that was appropriately scaled to recover a similar area expansion ratio for the cruise condition. The topology of the geometry faces has been simplified to aid surface mesh generation for the participants. This simplification includes fairing of the control surface gaps. The reference body

Fig. 2 C608 Configuration.

length is 1080 inches where meshes and geometry are also provided in inches.

The C608 freestream and boundary conditions are shown in Table 1. The C608 has propulsion and environmental control system (ECS) boundary conditions. The engine bypass exhaust is a semicircular region between the nozzle and aft deck and the ECS inlet is located in the wing root. There is an alternative Mach number propulsion boundary specification if a participant is unable to use a specified static pressure boundary condition. A number of participants reported difficulty with the ECS inlet and used the alternative boundary specification.

Table 1 C608 freestream and boundary conditions.

Condition	Description
1.4	Freestream Mach number
389.9	Freestream temperature, °R
53,200	Altitude, feet
109,776	Unit Reynolds number, per inch
10	Engine nozzle plenum total pressure to freestream static pressure ratio
2.4	Engine nozzle plenum total temperature to freestream static temperature ratio
2.4	Engine bypass exhaust total pressure to freestream static pressure ratio
2	Engine bypass exhaust total temperature to freestream static temperature ratio
2.6	Engine fan face static pressure to freestream ratio (recommended option)
1.4	ECS inlet static pressure to freestream ratio (recommended option)
0.4	Engine fan face Mach number (alternative to pressure)
0.35	ECS inlet Mach number (alternative to pressure)

Qualitative computational schlieren and surface pressures are shown in Fig. 3 to introduce features of the C608 that influence nearfield and ground sonic boom signatures shown later. The spade shaped nose creates a shock and expansion pair. The long slender nose creates a smooth compression until the canard, forward looking camera housing, and canopy. The wing leading edge, vortex generators behind the canopy, and ECS inlet create a rapid series of shocks and expansions. Inlet spillage creates a region of high pressure over the wing. The wing trailing edge, horizontal stabilator, aft deck, T-tail, engine plume, and tip vorticies result in extremely complex interactions and another rapid series of shocks and expansions.

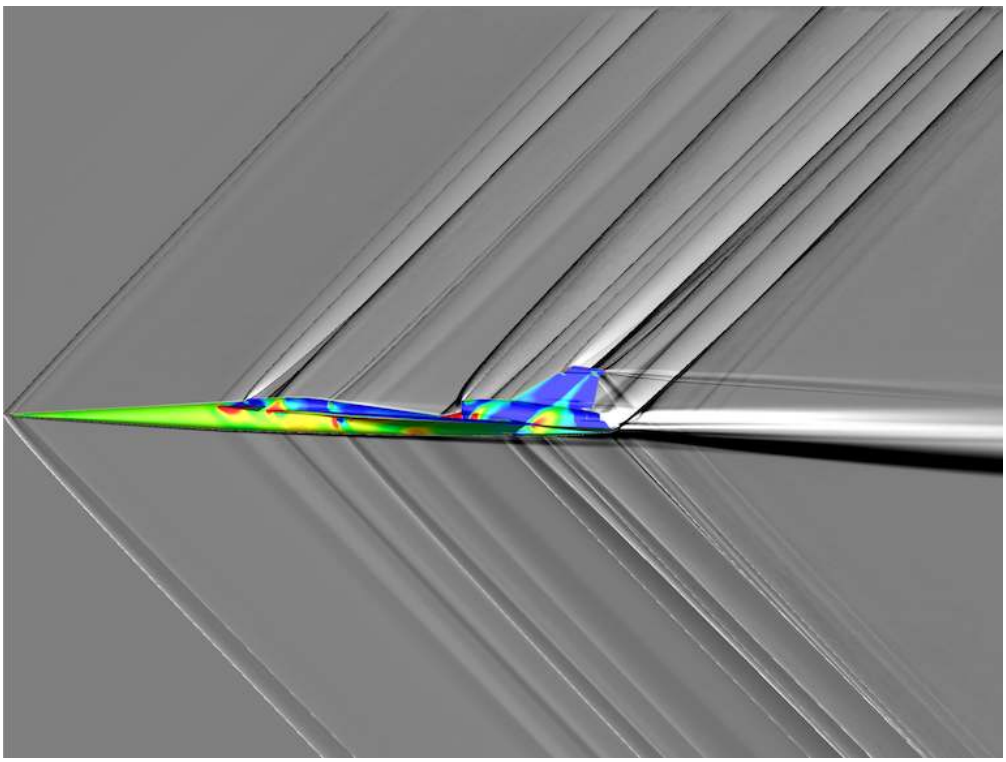

(a) Side view.

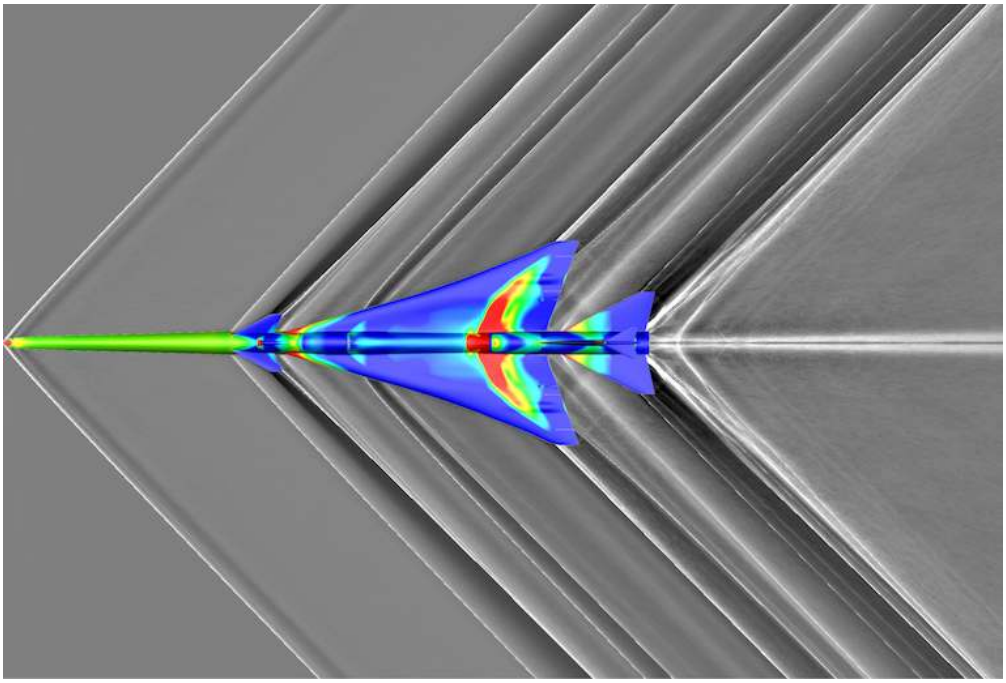

(b) Top-down view.

Fig. 3 Computational schleiren and surface pressures.

III. C608 Workshop-Provided Meshes

A set of meshes is provided to the participants to facilitate comparisons between CFD methods. The meshes are intended to be a family with consistently varying spatial resolution, but this is very difficult to attain for unstructured meshes that involve complex geometry with inconvenient face topology. The AIAA Drag Prediction Workshop series [21] identified the difficulty of constructing a consistent mesh family as a primary contribution to variation. Imperfect mesh refinement often complicates the interpretation of workshop results [22]. The unstructured workshop-provided meshes are constructed with mixed-elements and converted into tetrahedral-only versions. Mesh construction is separated into two phases. The first is the core grid, which is very near the aircraft to capture geometric complexity with unstructured mesh generation. An outer collar grid is wrapped around the core grid with a semistructured construction to efficiently align with the freestream Mach cone.

The core grids are created with HeldenMesh. There is limited information available for the HeldenMesh algorithm, which is inspired by VGRID [23, 24]. Ratnayake et al. [25] provide a detailed comparison between HeldenMesh and VGRID meshes. The ideal variation of element counts was not possible due to difficulties completing the mesh around the wing trailing edge. Different versions of HeldenMesh, and a range of boundary layer growth parameters, which departed from ideal, were used to overcome this difficulty. Six meshes were created, where element and vertex counts approximately double and spacing decreases by approximately 0.8 for each subsequent mesh. The degree of deviation from ideal are shown in the vertex and element counts of the mixed-element core mesh, Fig. 4a. Scale is a characteristic edge length of the mesh where a smaller scale is a finer mesh.

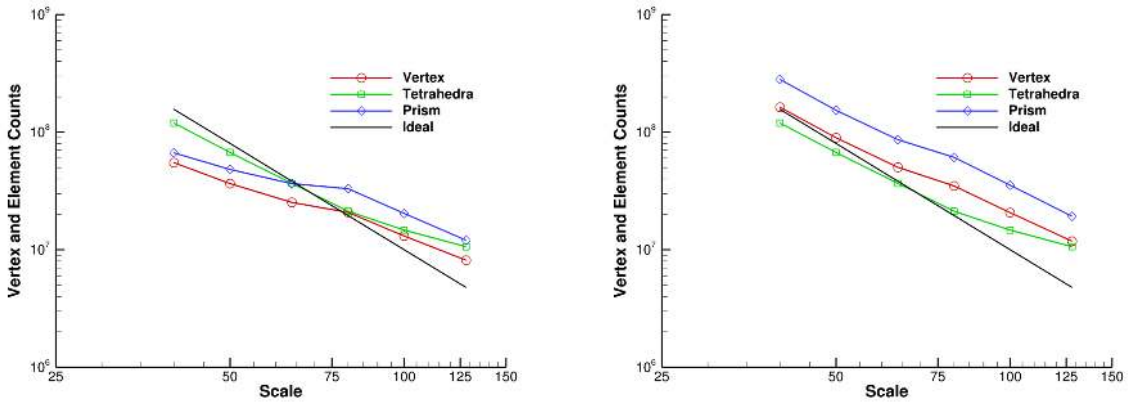

(a) Core mixed-element HeldenMesh. **(b) Complete mixed-element core and collar mesh.**

Fig. 4 C608 mesh vertex and element counts.

A freestream Mach aligned extruded collar mesh is created around the HeldenMesh core mesh via the method of Park et al. [26]. The vertex and element counts of the complete (core and collar) mixed-element (WS-Mixed) and tetrahedral-only (WS-Tet) meshes are plotted in Fig. 4b and listed in Table 2. Participants were instructed to run at least three of the provided meshes. This includes the finest mesh the participant had resources to compute and two coarser meshes. Submissions with the workshop-provided meshes was strongly encouraged to provide a comparison between CFD methods. Participants were also encouraged to provide their own meshes generated with best practices or solution-adaptive methods. For adaptive mesh methods, participants were expected to provide a submission on the finest meshes and two additional submissions on coarser intermediate adapted meshes to establish adaptive mesh convergence trends.

IV. Participant Groups

The groups contributing to the workshop are listed in Table 3. The group letter is the first part of the submission label used in the next section. Participants D and H only provided submissions for the Biconvex model. The D and H designations are skipped here for consistent participant codes between the Biconvex and C608 nearfield summaries. Some groups contain a single contributor, but most contain two or more collaborators. Government

Table 2 C608 viscous mesh families.

		WS-Mixed			WS-Tet
Scale	Vertices	Tetrahedra	Pyramids	Prisms	Tetrahedra
040	162,970,101	119,456,686	333,989	281,557,286	964,796,522
050	89,458,689	67,138,507	273,925	153,392,736	527,864,565
064	50,215,130	36,567,810	228,818	86,083,502	295,275,952
080	34,879,443	21,266,609	207,877	61,007,871	204,705,976
100	20,701,451	14,681,692	146,667	35,346,643	121,014,955
128	11,782,783	10,599,974	106,080	19,224,816	68,486,582

agencies, industry, academia, and vendors are represented. Most SBPW3 participants contributed to previous workshops. A number of new first-time participant groups represented commercial CFD vendors. Each group submitted results and prepared a presentation for the workshop. These presentations have been collected in the workshop website (`lbpw.larc.nasa.gov`). Participant A showed centerline pressure mapped to the offset from the freestream Mach cone to show the evolution of the signature at a range of body lengths and the geometric source of signature features. Participant B highlighted mesh element skewness near complex geometry and outer boundary layer prism-tetrahedra transition in the workshop provided meshes. Participant C presented an improved nonlinear solution technique and its potential to reduce simulation wall clock time. Participant E compared multiple mesh adaptation metrics to the workshop provided meshes. Participant F showed nearfield pressure unrolled on a cylinder to indicate the progression of the signature with offtrack angle (Φ) and identified the aft portion of the signal as containing the highest remaining error with Richardson extrapolation. Participant G highlighted the sensitivity of the signature to the ECS boundary conditions and initialization. Participant I showed numerical shadowgraphs and studied the stability of two pseudotime advancement schemes. Participant J showed the exhaust plume sensitivity to thermal conductivity. Participant K compared finite-element and finite-volume methods and showed details of the nearfield shock structure with unique density gradient visualizations. Participant L examined the sensitivity of turbulence model and computed the finest mixed-element workshop mesh with a cell-centered scheme. Participants M and N compared multiple reconstruction limiters and alternative boundary conditions on workshop-provided and adapted meshes. Participant O compared reconstruction limiter formulation and mesh element type. Participant P provided signatures but not a presentation.

Table 3 Participant groups.

Group	Organizations	Contributors
A	DLR	J. Kirz and R. Rudnik
B	Texas A&M	F. Carpenter and P. Cizmas
C	NASA	A. Elmiligui, M. Pandya, M. Carter, B. Diskin, and S. Nayani
E	Boeing	T. Michal, T. Maggee, J. Krakos, and D. Lazzara
F	STC and NASA	W. Spurlock, A. Aftosmis, and M. Nemec
G	NASA	J. Jensen, J. Duensing, M. Piotrowski, J. Housman, and C. Kiris
I	Siemens Digital Industry Software	C. Nelson, O. Tong, and M. Castillo
J	Boom Technology	E. Fabiano
K	ANSYS Canada	I. Ozcer, J. Stokes, L. Munholand, and K. Zore
L	Metacomp Technologies	A. Potturi
M	NASA	M. Park
N	INRIA	A. Loseille and F. Alauzet
O	JAXA	H. Ishikawa, S. Koganezawa, and Y. Makino
P	Lockheed Martin	M. Buonanno

V. Nearfield Signatures

A majority of the submissions were collected from the participants before the workshop. Some participants exercised an option to update or augment their submission after the workshop. An extraction macro was provided to the participants to encourage uniform data submission. Nearfield signatures were requested in 2° increments from 0–180° Φ at a three body length radius from the nose of one half of the symmetric configuration. To enable analysis, the participant submissions were corrected to eliminate formatting errors. Participants were contacted for clarification when the extraction location was incorrect, signatures were incomplete, significant differences existed between submissions of the same participant, or boundary conditions were suspect.

The submissions are listed in Table 4 where a characteristic length is estimated as $h = 10^{7/3}N^{-1/3}$ and the number of control volumes are N. The h is scaled so a mesh of 10 million control volumes has an $h = 1$. The majority of CFD simulations include a turbulence model. The Spalart Almarras [27] (SA) turbulence model optionally including a Rotational/Curvature Correction (RC) [28] and Quadratic Constitutive Relation (QCR) [29] is the most common. Any submissions using the negative form of SA model [30] are also referred to as SA. The Shear Stress Transport (SST) of Menter [31] is used in the remaining turbulent cases.

Participant A used TAU [32, 33] with the SA turbulence model. Participant B used UNS3D [34] and the SST turbulence model with weighted least-squares (LSQ) and Green-Gauss (GG) gradient reconstruction. Most Participant B cases used the Harten [35] modification of the Roe [36] flux (RoeH), and one case used a modified Roe (RoeM) by Kim et al. [37]. Participant C used the mixed-element formulation USM3D_ME [38] with the SA turbulence model. Participant E used BCFD [39] with the EPIC [40] adaptive mesh mechanics. The EPIC Goal-Mixed meshes are constructed with a goal-based metric [41], and the L2-Mixed are constructed with a multiscale metric [42] to control an L2 interpolation error of the Mach number field. Participants E, M, and P used the FUN3D [43] solver. FUN3D-Roe used the Roe flux. FUN3D Grad-Mixed meshes use a solution jump indicator [44] and FUN3D Goal-Mixed meshes use an adjoint indicator [45, 46]. Both Grad-Mixed and Goal-Mixed FUN3D meshes use the frozen boundary layer method of Park and Carlson [47].

Participant F used the Cart3D [48–50] inviscid solver with adaptive Cartesian cut cells to control estimated error at nearfield sensor locations. Participant G used the overset curvilinear and polyhedral versions of LAVA [51]. The structured overset curvilinear version of LAVA used a third-order Roe scheme with a blended upwinding scheme for the meanflow and SA model. The polyhedral version of LAVA used SA with the Advection Upstream Splitting Method by Pressure-based Weight functions (AUSMPW+) [52] and minmod limiter for the standard inlet boundary conditions and the optional specified Mach (MachBC) inlet boundary conditions.

Participant I used Simcenter STAR-CCM+ [53] with the SST turbulence model. Participants J and L used CFD++ version 18.1 [54], where Participant J used SA-RC and Participant L used SST. Participant K used the Galerkin finite-element method HALO3D described by Seguin et al. [55] with the SA turbulence model and Fluent [56] with the SST turbulence model.

Participant M used FUN3D-Roe and FUN3D-LDRoe with low-dissipation Roe flux of Nishikawa and Liu [57]. FUN3D-VL used a van Leer limiter [58] and FUN3D-BJ used a Barth-Jespersen limiter [59]. FUN3D-MachBC used the alternative specified Mach number boundary conditions for engine and ECS inlets. The L2-Tet Mach multiscale mesh adaptation process is described in Park et al. [60] and the mesh mechanics for complex geometry are described in Park et al. [61]. Participant N used the HLLC flux [62] with the Wolf solver and Mach multiscale mesh adaptation L2-Tet [63]. Participant O used the FaSTAR [64, 65] flow solver with Venkatakrishnan limiter [66] and HLLEW (Harten-Lax-van Leer-Einfeldt-Wada) flux [67]. A structured laminar UPACS [68] collar grid was combined with an unstructured FaSTAR mesh as described by Ishikawa et al. [69] for the Participant O results FaSTAR+UPACS. Participant P used FUN3D-DLDFSS with a Dissipative Low-Diffusion Flux-Splitting Scheme [70].

The submissions listed in Table 4 form an ensemble shown in Fig. 5. The centerline and three offtrack Φ are selected to provide an overview of the C608 nearfield environment. Examining the pointwise sample mean and standard deviation of these signatures highlights the portions of the signature with a large variation and portions with a small variation, as shown by the black error bars in Fig. 5. A similar technique is used in wind tunnel testing, where signatures measured at different locations in a wind tunnel test section are spatially averaged to reduce the impact of disturbances in the tunnel [71, 72].

The sample mean and standard deviation are computed by linearly interpolating the finest-mesh submission from each case to a common set of points with 0.5 inch resolution or 2160 points per body length. This variation among the ensemble of measurements is expressed as a standard deviation at each interpolated point. The interpolated mean is shown as a line, and the standard deviation is shown as an error bar with a height of one standard deviation above and

below the mean. Multiple shocks at $X = 4250$ inches on the centerline merge into a single shock offtrack. The ECS inlet boundary condition increased variation at $X = 3750$ inches. The horizontal stabilizer ($X = 4125$ inches) and aft deck lip shock ($X = 4275$ inches) positions have increased variation. A reduction in sample standard deviation from SBPW1 [1] and SBPW2 [2] is observed in the SBPW3 ensemble.

Table 4 C608 submissions.

Case	Code	Model	Mesh	Millions of Control Volumes (h)
AA	TAU	SA	WS-Mixed	50.2(0.58), 34.9(0.66), 20.7(0.78), 11.8(0.95)
AB	TAU	SA	WS-Tet	34.9(0.66), 20.7(0.78), 11.8(0.95)
BB	UNS3D-RoeH-LSQ	SST	WS-Mixed	11.8(0.95)
BC	UNS3D-RoeM-LSQ	SST	WS-Mixed	11.8(0.95)
BD	UNS3D-RoeH-GG	SST	WS-Mixed	50.2(0.58), 34.9(0.66), 20.7(0.78), 11.8(0.95)
CA	USM3D_ME	SA	WS-Mixed	220.5(0.36), 122.7(0.43), 82.3(0.50), 50.0(0.58), 29.8(0.69)
EA	BCFD	SA	WS-Mixed	220.5(0.36), 122.7(0.43), 82.3(0.50), 50.0(0.58), 29.8(0.69)
EB	BCFD	SA	Goal-Mixed	64.0(0.54), 32.0(0.68), 16.0(0.85), 8.0(1.08), 4.0(1.36), 2.0(1.71)
EC	BCFD	SA	L2-Mixed	256.0(0.34), 128.0(0.43), 64.0(0.54), 32.0(0.68), 16.0(0.85), 8.0(1.08), 4.0(1.36), 2.0(1.71)
ED	FUN3D-Roe	SA	Grad-Mixed	21.4(0.78)
EE	FUN3D-Roe	SA	Goal-Mixed	163.4(0.39), 136.5(0.42)
FA	Cart3D	Inviscid	Cartesian	29.6(0.70), 14.2(0.89), 7.1(1.12)
GA	LAVA-Curvilinear	SA	Overset	450.9(0.28), 127.4(0.43), 40.3(0.63)
GC	LAVA-Polyhedral	SA	Polyhedral	140.0(0.41), 94.4(0.47), 27.7(0.71)
GD	LAVA-Polyhedral-MachBC	SA	Polyhedral	140.0(0.41)
IA	STAR-CCM+	SST	WS-Mixed	82.3(0.50), 50.0(0.58), 29.8(0.69)
JA	CFD++	SA-RC	WS-Mixed	82.3(0.50), 50.0(0.58), 29.8(0.69)
KA	HALO3D	SA	WS-Mixed	34.9(0.66), 20.7(0.78), 11.8(0.95)
KB	Fluent	SST	WS-Mixed	82.3(0.50), 50.0(0.58), 29.8(0.69)
LA	CFD++	SST	WS-Mixed	401.0(0.29), 220.5(0.36), 122.7(0.43), 82.3(0.50), 50.0(0.58), 29.8(0.69)
LD	CFD++	SA	WS-Mixed	401.0(0.29), 220.5(0.36), 122.7(0.43), 82.3(0.50), 50.0(0.58), 29.8(0.69)
LE	CFD++	SA-RC-QCR	WS-Mixed	401.0(0.29), 220.5(0.36), 122.7(0.43), 82.3(0.50), 50.0(0.58), 29.8(0.69)
MA	FUN3D-VL	SA	WS-Mixed	163.0(0.39), 89.5(0.48), 50.2(0.58), 34.9(0.66), 20.7(0.78), 11.8(0.95)
MC	FUN3D-Roe-VL-MachBC	SA	WS-Mixed	163.0(0.39), 89.5(0.48), 50.2(0.58), 34.9(0.66), 20.7(0.78), 11.8(0.95)
MD	FUN3D-Roe-VL-MachBC	SA	L2-Tet	55.6(0.56), 28.0(0.71), 14.1(0.89), 7.2(1.12), 3.7(1.39)
ME	FUN3D-LDRoe-VL-MachBC	SA	L2-Tet	55.6(0.56), 28.0(0.71), 14.1(0.89), 7.2(1.12), 3.7(1.39)
MF	FUN3D-Roe-BJ-MachBC	SA	L2-Tet	55.7(0.56), 28.1(0.71), 14.2(0.89), 7.2(1.12), 3.7(1.39)
NB	Wolf-HLLC-V4	SA	L2-Tet	26.4(0.72), 13.1(0.91), 6.6(1.15), 3.3(1.45)
OA	FaSTAR	SA	WS-Mixed	89.5(0.48), 50.2(0.58), 34.9(0.66), 20.7(0.78), 11.8(0.95)
OD	FaSTAR+UPACS	SA+Laminar	Overset	88.2(0.48), 74.0(0.51), 65.1(0.54)
PA	FUN3D-DLDFSS-VL	SA	WS-Mixed	50.2(0.58), 34.9(0.66), 20.7(0.78)

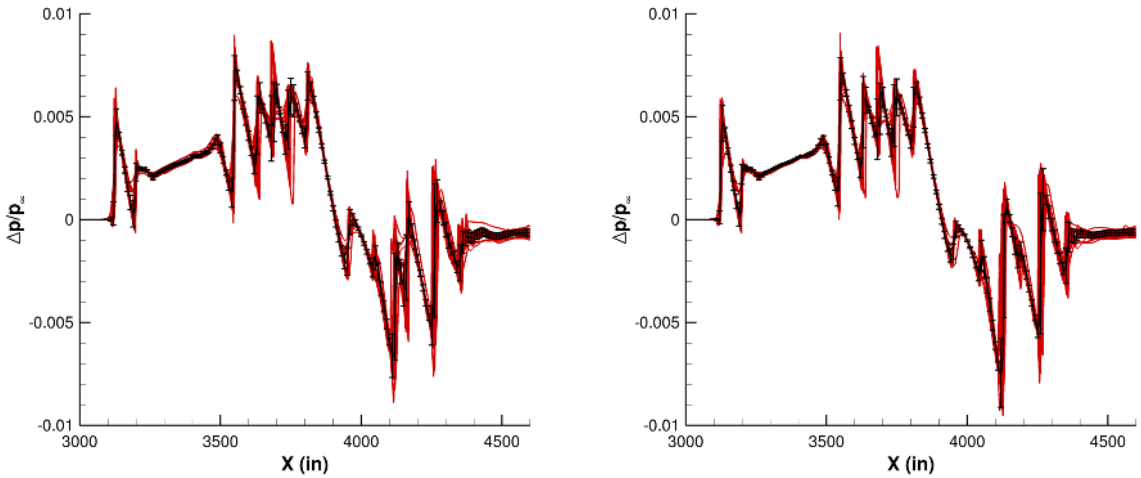

(a) $\Phi = 0°$.

(b) $\Phi = 10°$.

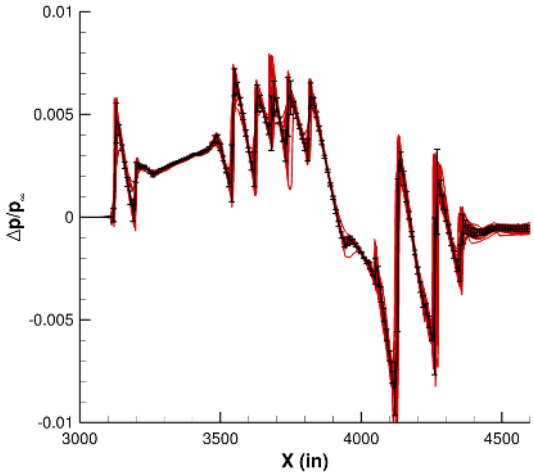

(c) $\Phi = 20°$.

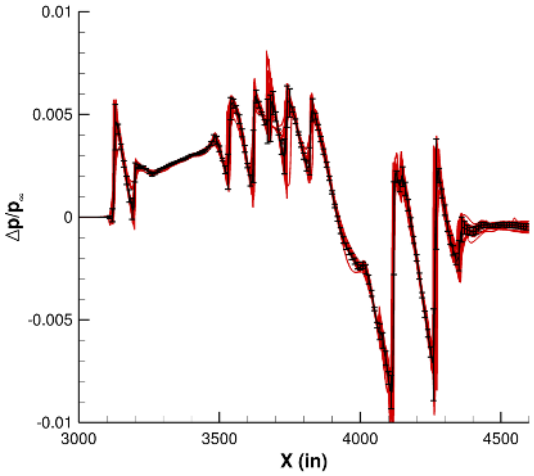

(d) $\Phi = 30°$.

Fig. 5 Nearfield signatures with one standard deviation error bars.

VI. Ground Signatures

The sBOOM code of Rallabhandi [73, 74] solves an augmented Burgers' equation to propagate nearfield signatures to the ground. This is the atmospheric propagation step in Fig. 1. Version 2.82 of sBOOM is used in this summary.

The C608 is at 53,200 ft altitude in a no-wind US Standard Atmosphere [75] and the atmospheric humidity model from ANSI S1.26, Annex C [76]. The specified Mach number is 1.4. To reduce computational cost. the meshes are typically truncated or the mesh is coarsened before the aft pressure signature returns to freestream. Participants provided extracted pressure between different forward and aft locations.

In order to decrease variation, the signatures are windowed to reduce the differences in the downstream plume extent. Before propagation, the initial and final delta pressures are linearly ramped to zero, windowing the submission to focus the statistics on the model. The fore and aft signature ramping is applied uniformly based on the freestream Mach cone extending from the nose of the model, see Park and Morgenstern [7] for details. The forward portion of each signature is ramped from zero to the submitted pressure between -0.2 and -0.1 body lengths ahead of the freestream Mach cone. The aft portion of each signature is ramped from the submitted pressure to zero between 1.5 and 2.5 body lengths behind the freestream Mach cone. The windowed nearfield signature is padded with zeros to have a full extent of -0.5 to 3.2 body lengths from the freestream Mach cone.

Like the results of any finite-difference method [77], the ground signatures predicted by sBOOM have a sensitivity to the number of points used to discretize the signature [73]. For example, to verify the consistency of the sBOOM finite difference method, a series of uniformly-refined meshes are used in Park and Morgenstern [7]. This reference also examines frequency spectra showing that sBOOM mesh refinement has the greatest impact on the higher frequencies of the ground signature. The sBOOM discretization uses 36,000 points to propagate the signature, which is 9,730 points per body length or nine points per inch in the nearfield. This spatial resolution near the aircraft results in 147 kHz temporal resolution at the ground. Based on previous studies [7], noise measures are expected to be within 0.1 dB of thier asymptotic value at this resolution.

Acoustic disturbance sources distributed in the spanwise direction reach a nearfield extraction location after traveling a longer distance than the centerline disturbances. This extra distance results in wave superposition at a more aft location that alters the signature shape. This signature change with extraction distance is known as nearfield interference. When signatures are extracted sufficiently far from the model, a farfield propagation technique (sBOOM) is usable without farfield correction [78] because the acoustic sources appear to come from a single line. This workshop extracts nearfield signatures at a constant radius from the nose. An investigation of the impact of nearfield interference was pursed in SBPW1 and SBPW2 and indicated that the three body length extraction distance used here is acceptable.

The nearfield submissions propagated to the ground are shown in Fig. 6 for centerline and offtrack propagation angles. The differences in ECS boundary condition implementation are seen at $T = 0.4$ sec. Variation increases after the initial pressure rise of the bow shock, above 4 Pa, until the peak pressure difference. The variation is smallest in the main expansion in the center of the ground signature. Variation increases again in the tail compression, where there is disagreement in pressure difference magnitude and shape of the initial tail compression.

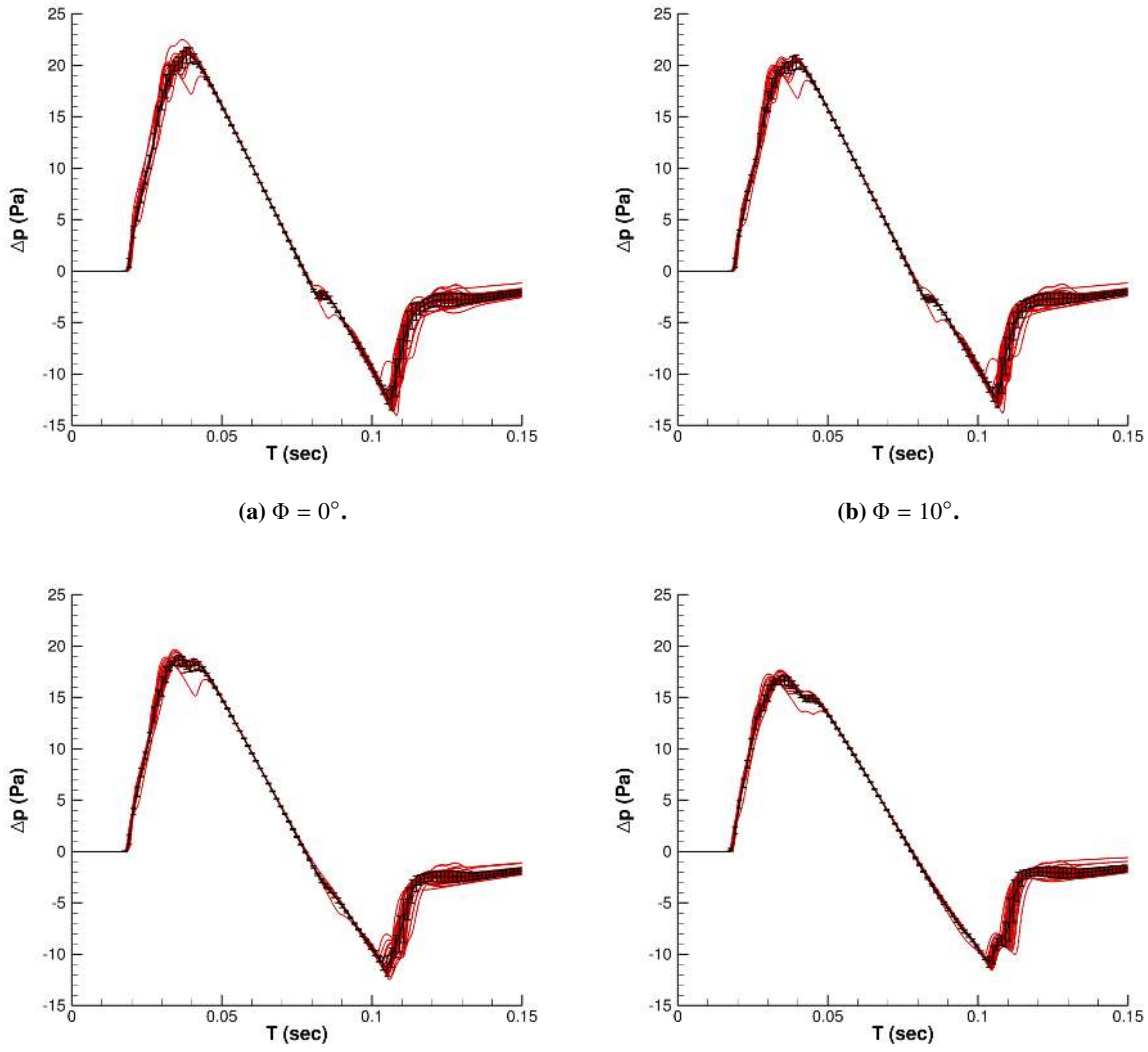

(a) $\Phi = 0°$. **(b)** $\Phi = 10°$.

(c) $\Phi = 20°$. **(d)** $\Phi = 30°$.

Fig. 6 Ground signatures with one standard deviation error bars.

VII. Loudness Carpet

Sonic boom loudness and annoyance are an inherently subjective experience. Many noise descriptors have been evaluated as loudness predictors of sonic booms in human experiments, see Leatherwood et al. [79]. The Mark VII perceived level (PL) of Stevens [80] is used to compare submissions because it is correlated with loudness and annoyance in multiple experiments [79, 81]. The method of Shepherd and Sullivan [82] is used to calculate PL from ground signatures.

The PL loudness carpet is shown in Fig. 7. The black error bars are based on one standard deviation above and below the mean of each submission group. PL is an extremely sensitive measure, which is particularly sensitive to the high-frequency content of the ground signature (i.e., the nose and tail shocks in Fig. 6 with the highest sample standard deviation). The variation in Fig. 7 is decomposed into principle components and compared to SBPW1 and SBPW2 later in this summary.

All fine-mesh submissions are shown in Fig. 7a. The mean carpet is louder near the centerline and transitions to a lower PL between 10–22° Φ. These fine-mesh submissions are split by mesh source, where Fig. 7b are workshop-provided mesh submissions and Fig. 7c are participant-generated mesh submissions. The workshop-provided mesh submission sample standard deviation is lower near the centerline, below 16° Φ. The variation of the workshop-provided mesh submissions increases for larger offtrack angles. The variation of the participant-generated mesh submissions is highest on the centerline with a reduction in variation to a minimum at 26–34° Φ.

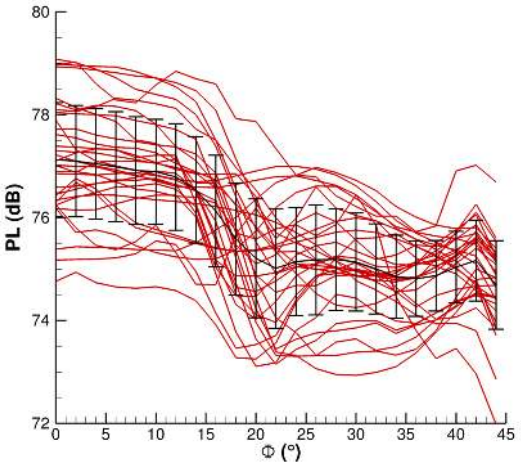

(a) All fine-mesh submissions.

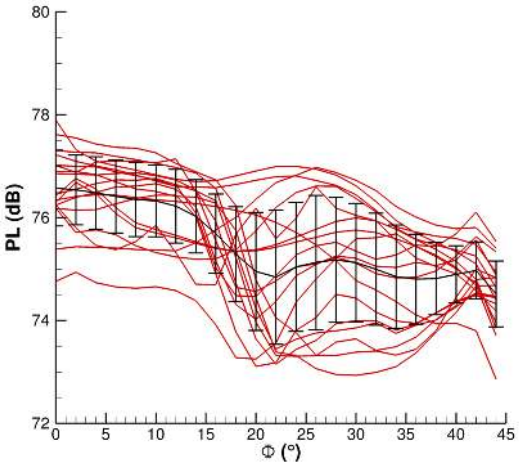

(b) Fine workshop-provided mesh submissions.

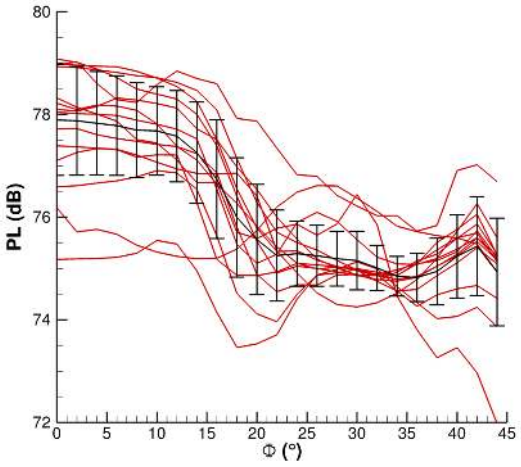

(c) Fine participant-generated mesh submissions.

Fig. 7 Loudness carpet with one standard deviation error bars based on all fine-mesh submissions.

VIII. Functional Principal Component Analysis

The functional principal component analysis technique of functional data analysis [83] is applied to extract shape variation of sonic boom carpets. This analysis augments the previous use of the sample mean and standard deviation to extract pointwise magnitude variation from submissions and their derived data. The correlation is shown in Fig. 8. PL is strongly correlated at 0–15° and 25–35° Φ. PL is negatively correlated between 0–15° and 30–35° Φ, meaning that the variation from the mean is of opposite sign between these offtrack angle regions. The eigenvalues of the covariance matrix are computed to reveal the principal components of variability.

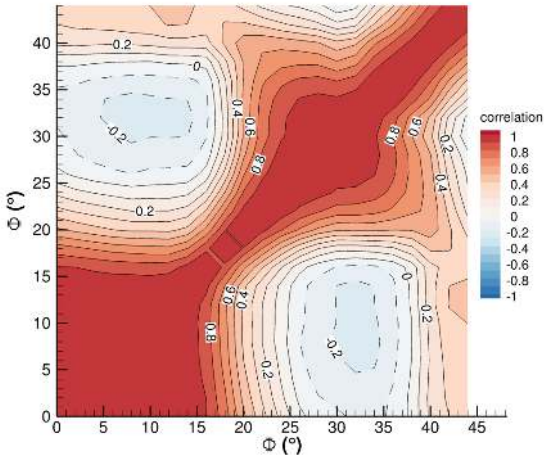

Fig. 8 Loudness carpet Φ correlation of all fine-mesh submissions.

The first four components of variability are shown in Fig. 9, which include 97.5% of the total variability. Each of these components is a signed perturbation from the mean, labeled Upper, and is shown with its refection, labeled Lower. The remaining modes are all below 1% of the total variability. The first mode, accounting for 50.2% of the variability (Fig. 9a), has most variation below 30° and has a similar pattern to the participant-generated mesh submissions, Fig. 7c. The first mode is of the same sign above and below a minimum variation at 32°Φ. The second mode, accounting for 35.7% of the variability (Fig. 9b), is primarily offtrack variation. This mode is slightly below the mean for offtrack angles smaller than 17° Φ and above the mean for higher offtrack angles. The second mode has a similar pattern to the workshop-provided mesh submissions, Fig. 7b. The third mode with 7.6% of the variability is a high frequency mode with a peak above 35°, Fig. 9c. The fourth mode with 4.1% of the variability is a high frequency mode, Fig. 9d.

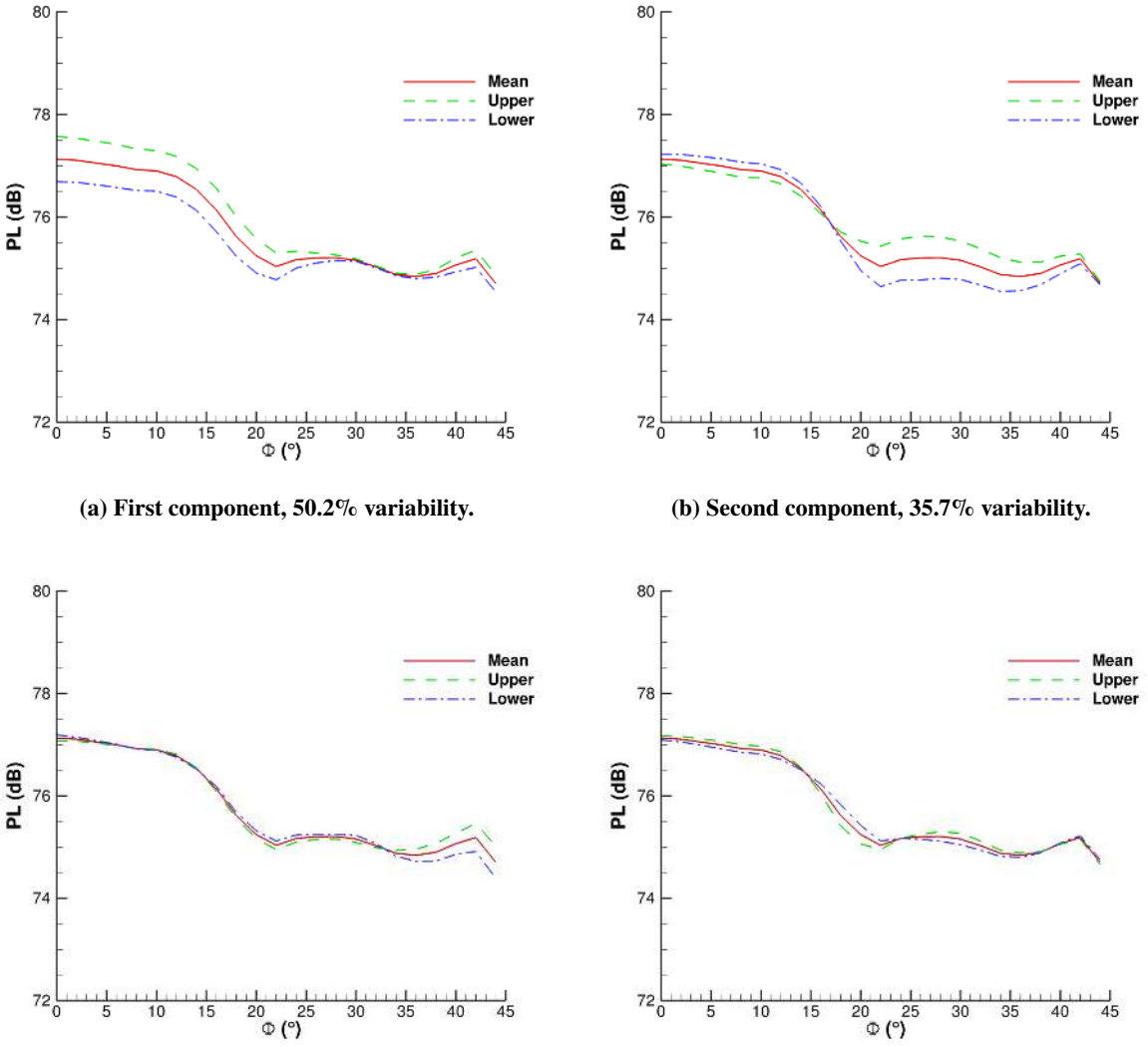

(a) First component, 50.2% variability.

(b) Second component, 35.7% variability.

(c) Third component, 7.6% variability.

(d) Forth component, 4.1% variability.

Fig. 9 Variability components of the loudness carpet above 1%.

IX. Mesh Convergence

The mesh convergence of PL is shown in Fig. 10 at four Φ angles. The characteristic length is estimated as $h = 10^{7/3}N^{-1/3}$ where the number of control volumes is N, and the h is scaled so a mesh of 10 million control volumes has an $h = 1$. The gross trend of many submissions is quieter with increased mesh resolution. The variation between submissions does not appear to reduce with increased mesh resolution.

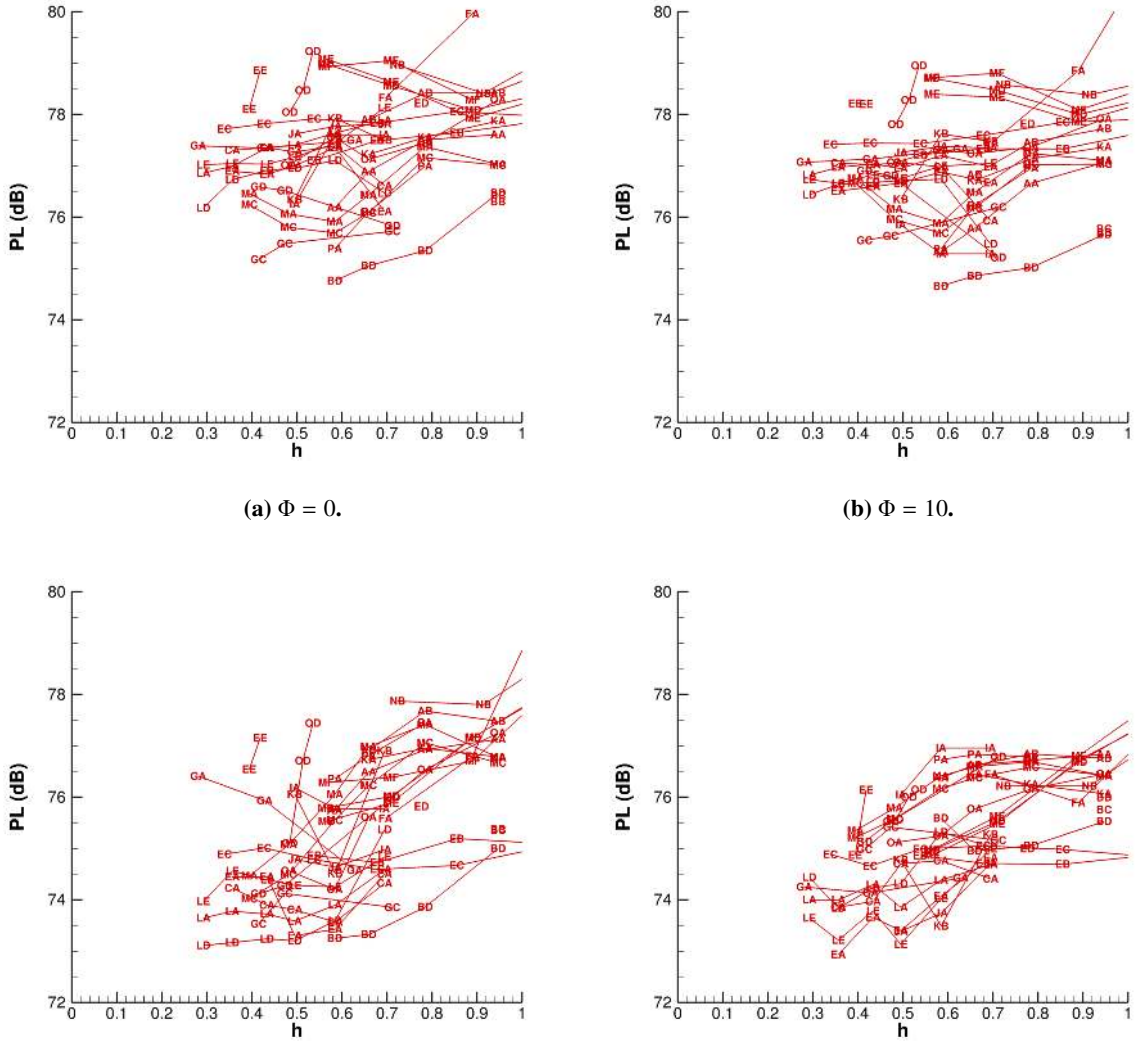

(a) Φ = 0**.** **(b)** Φ = 10**.**

(c) Φ = 20**.** **(d)** Φ = 30**.**

Fig. 10 Mesh convergence of PL.

X. Sonic Boom Workshop Progress

Ground PL and sones carpets are shown for similar class vehicles from the three sonic boom workshops in Fig. 11. Stevens [80] defines the sone unit as the perceived magnitude (loudness or noisiness) of a reference signal at a pressure level of 32 dB. PL is related to total sones by $PL = 32 + 9\log_2(\text{Sones})$. The LM1021 was a wind tunnel model with flowthrough nacelles that was an optional case from SBPW1 [1]. The C25F was a notional low boom flight demonstrator model with flowthrough nacelle that was a required case of SBPW2 [2]. The C25P was a variant of the C25F with powered boundary conditions that was an optional SBPW2 case. The C608 is the focus of this SBPW3 summary. The LM1021 lacked a mesh refinement study; all LM1021 submissions are shown in Fig. 11. The C25F, C25P, and the C608 cases included mesh refinement studies; the fine-mesh C25F, C25P, and C608 submissions are shown in Fig. 11.

The progression of the workshop series shows a clear downward trend in PL and sones for these complex configurations. There is also an increase in the number of submissions for each subsequent workshop configuration. Complexity increased due to increased detail for the progression of models. The C25P introduced propulsion boundary conditions and the C608 includes both propulsion boundary conditions and ECS boundary conditions. Signature loudness is more difficult to accurately predict for quieter configurations than for louder configurations because an equal magnitude error has a larger relative impact on a smaller sone or PL signature. The logarithmic transform of sones to PL expands the differences of quiet signatures more than loud signatures, which can be seen by comparing Fig. 11a and Fig. 11b. The C608 is the quietest and has the lowest variation of the workshop cases, which is more clearly seen in sones. These trends document the significant and consistent increase in skill of the international nearfield sonic boom community. Each workshop contained first-time participants, which indicates that the community is engaged in effective knowledge stewardship and communication to maintain reductions in variation while increasing complexity.

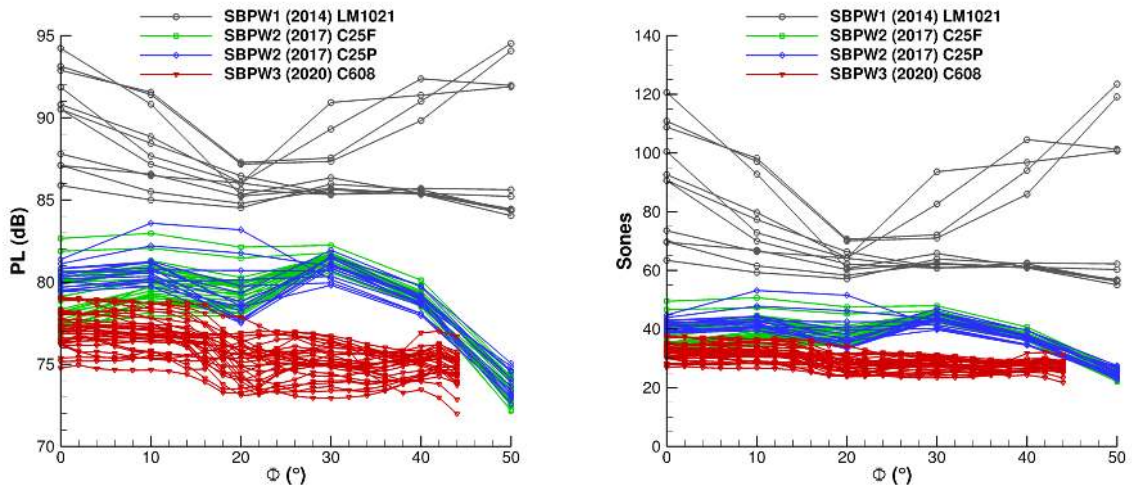

(a) PL. **(b) Sones.**

Fig. 11 Progress made in three sonic boom workshops.

XI. Conclusions and Recommendations

A summary and statistical analysis is provided for the nearfield Computational Fluid Dynamics (CFD) submissions to the Third AIAA Sonic Boom Workshop (SBPW3) with a focus on the C608 preliminary configuration of a low-boom demonstrator vehicle. This is the most complex and complete configuration in the Sonic Boom Workshop series with multiple control surfaces and boundary conditions for the environmental control system (ECS), engine nozzle, and engine bypass. The C608 is representative of the Lockheed Martin X-59 QueSST for NASA's Low-Boom Flight Demonstrator program, but caution should be exercised applying workshop simulations to the performance of the final X-59 design, due to differences in geometry and boundary conditions between the C608 and the X-59. Computational schlieren is shown for the C608 to introduce the configuration details of the C608 that influence nearfield CFD signatures.

SBPW3 saw an influx of commercial CFD vendor participation. The first use of a finite-element method by a participant in SBPW3 may open the door to lower dissipation or higher order schemes in sonic boom prediction. The trend toward larger meshes in the workshop series has continued; the C608 had double the vertex and element counts of the C25P and 18% more than the C25F from the previous workshop SPBW2 [2]. SBPW3 submissions included a significantly higher percentage of adaptive mesh submissions than the previous workshop: 7% for the C25P versus 29% for the C608. The fine-mesh sample standard deviation of the nearfield signatures appears lower for the C608 than the C25F or C25P indicating that consistency has improved between the two workshops.

The nearfield CFD submissions were propagated to the ground with the sBOOM augmented Burgers' equation method [73] and the Perceived Loudness (PL) measure [80] was computed. The fine-mesh ground signature sample standard deviation is largest for the tail compression and variation in shape is also observed. The PL sample mean and standard deviation at each offtrack angle Φ was computed to augment the sonic boom carpets. A transition occurs in the carpets at 15–20° Φ from a louder PL near the centerline and a quieter PL offtrack. The submissions with the workshop-provided meshes were quieter than the mean PL of the entire ensemble and had lower variation near the centerline. The PL variation of the submissions with the workshop-provided meshes grew for larger offtrack angles. The participant generated meshes (including adapted meshes) were louder with larger variation near the centerline with the lowest variation at $\Phi = 35°$. Functional principle component analysis extracted the first four modes of variation that contained 97.5% of the total variability. The first mode had similarities with the participant-generated mesh submissions, and the second had similarities with the workshop-provided mesh submissions. A plot of correlation provided the relation between variation at different Φ.

Uniformly-refined meshes were provided to participants, but vertex and element counts indicate that the meshes deviate from an ideal family of meshes. Ideal mesh refinement for unstructured meshes on a complex configuration is an open research problem for the mesh generation community. With this caveat, uniform mesh refinement remains an important tool for verifying CFD methods. The impact of nearfield CFD mesh refinement on PL was shown at several Φ locations. Participant generated and adapted meshes were also requested at a number of sizes to study trends. The general trend was quieter PL with mesh refinement. Variation did not reduce with mesh refinement, which reinforces the difficulty of simulating configurations with significant viscous effects. The viscous submissions for the C25P with propulsion boundary conditions and C25F with flowthrough nacelle had larger variation with less consistent mesh refinement trends than inviscid simulations [2].

Comparing configurations from previous workshops to the C608 showed a reduction in PL and PL variation in the workshop series. This clearly demonstrates the progress made by the international sonic boom prediction community to lower variation, including a number of first-time participant groups for each workshop. The nearfield signature sample standard deviation appears to reduce more than PL variation, which confirms the C608 is the most difficult nearfield CFD configuration from the sonic boom workshop series. The SBPW3 participants may have reached a useful level of variation on a full configuration with many realistic features and a loudness approaching the range of published PL design targets [15, 84, 85].

Lowering the variation in the nearfield CFD further may not be relevant due to the uncertainty in the entire system [86]. Therefore, the possibility exists that another nearfield CFD workshop in the same format could produce diminishing returns. In addition, maintaining a three year workshop spacing between the first three workshops may conflict with the possible flight test window of the X-59. On the other hand, organizing the next nearfield CFD workshop after the final configuration and flight data are available would provide a unique opportunity for validation to flight data. Before flight data are available, conference special sessions could focus on detailed aspects of CFD modeling and ensure the sonic boom community is prepared for a validation campaign. Mesh adaptation, the influence of integrated propulsion effects, and accuracy/efficiency improvements to CFD are good candidates. There is also the opportunity to shadow or augment the current X-59 review process and develop certification by analysis methods and process.

Acknowledgments

The authors would like to thank the entire SBPW3 organizing committee, participants, and attendees. The discussions during the workshop and in the hallways helped to craft the content and recommendations of this summary. The C608 configuration was developed by Lockheed Martin. Norma Farr, Scott Brynildsen, and Michael Wiese (NASA Langley Geometry Laboratory) prepared the C608 geometry and HeldenMesh input files. Alex Kleb (University of Michigan, former NASA Langley Intern) assessed the notice of intent submissions, prepared the C608 workshop-provided meshes, performed C608 geometry assessment, and provided feedback on the summary. Jochen Kirz (DLR) and Todd Michal (Boeing) provided feedback on the workshop-provided meshes.

The suggestions provided by SBPW1 and SBPW2 participants contributed greatly to the success of SBPW3. Joe Derlaga (NASA Langley) and Bil Kleb (NASA Langley) provided helpful feedback. Sriram Rallabhandi (NASA Langley) provided the atmospheric propagation tool sBOOM and assistance on its use. Alexandra Loubeau (NASA Langley) provided the noise level calculation tool, guidance on its use, and detailed background on noise levels. This work is supported under the Commercial Supersonic Transport Project of the NASA Fundamental Aerodynamics Program.

References

[1] Park, M. A., and Morgenstern, J. M., "Summary and Statistical Analysis of the First AIAA Sonic Boom Prediction Workshop," *AIAA Journal of Aircraft*, Vol. 53, No. 2, 2016, pp. 578–598. doi:10.2514/1.C033449.

[2] Park, M. A., and Nemec, M., "Near Field Summary and Statistical Analysis of the Second AIAA Sonic Boom Prediction Workshop," *AIAA Journal of Aircraft*, Vol. 56, No. 3, 2019, pp. 851–875. doi:10.2514/1.C034866.

[3] Carter, M. B., and Park, M. A., "Near Field Summary and Analysis of the Third AIAA Sonic Boom Prediction Workshop Shock-Plume Interaction Case," AIAA AVIATION 2020 American Institute of Aeronautics and Astronautics, Reston, VA (submitted for publication).

[4] Rallabhandi, S. K., and Loubeau, A., "Summary of Propagation Cases of the Third AIAA Sonic Boom Prediction Workshop," AIAA AVIATION 2020 American Institute of Aeronautics and Astronautics, Reston, VA (submitted for publication).

[5] Hemsch, M. J., "Statistical Analysis of Computational Fluid Dynamics Solutions from the Drag Prediction Workshop," *AIAA Journal of Aircraft*, Vol. 41, No. 1, 2004, pp. 95–103.

[6] Park, M. A., Aftosmis, M. J., Campbell, R. L., Carter, M. B., Cliff, S. E., and Bangert, L. S., "Summary of the 2008 NASA Fundamental Aeronautics Program Sonic Boom Prediction Workshop," *AIAA Journal of Aircraft*, Vol. 51, No. 3, 2014, pp. 987–1001. doi:10.2514/1.C032589.

[7] Park, M. A., and Morgenstern, J. M., "Summary and Statistical Analysis of the First AIAA Sonic Boom Prediction Workshop," AIAA Paper 2014–2006, 2014.

[8] Park, M. A., and Nemec, M., "Near Field Summary and Statistical Analysis of the Second AIAA Sonic Boom Prediction Workshop," AIAA Paper 2017–3256, 2017.

[9] Tinoco, E. N., Brodersen, O. P., Keye, S., Laflin, K. R., Feltrop, E., Vassberg, J. C., Mani, M., Rider, B., Wahls, R. A., Morrison, J. H., Hue, D., Roy, C. J., Mavriplis, D. J., and Murayama, M., "Summary Data from the Sixth AIAA CFD Drag Prediction Workshop: CRM Cases," *AIAA Journal of Aircraft*, Vol. 54, No. 4, 2018, pp. 1352–1379. doi:10.2514/1.C034409.

[10] Derlaga, J. M., and Morrison, J. H., "Statistical Analysis of the Sixth AIAA Drag Prediction Workshop Solutions," *AIAA Journal of Aircraft*, Vol. 55, No. 4, 2018, pp. 1388–1400. doi:10.2514/1.C034938.

[11] Rumsey, C. L., Slotnick, J. P., and Sclafani, A. J., "Overview and Summary of the Third AIAA High Lift Prediction Workshop," *AIAA Journal of Aircraft*, Vol. 56, No. 2, 2019, pp. 621–644. doi:10.2514/1.C034940.

[12] DeBonis, J. R., Oberkampf, W. L., Wolf, R. T., Orkwis, P. D., Turner, M. G., Babinsky, H., and Benek, J. A., "Assessment of Computational Fluid Dynamics and Experimental Data for Shock Boundary-Layer Interactions," *AIAA Journal*, Vol. 50, No. 4, 2012, pp. 891–903. doi:10.2514/1.J051341.

[13] "Civil Aircraft Sonic Boom," Code of Federal Regulations, Title 14, Part 91.817, 2011.

[14] Liebhardt, B., Linke, F., and Dahlmann, K., "Supersonic Deviations: Assessment of Sonic-Boom-Restricted Flight Routing," *AIAA Journal of Aircraft*, Vol. 51, No. 6, 2014, pp. 1987–1996. doi:10.2514/1.C032591.

[15] Henne, P. A., "Case for Small Supersonic Civil Aircraft," *AIAA Journal of Aircraft*, Vol. 42, No. 3, 2005, pp. 765–774. doi:10.2514/1.5119.

[16] Sakata, K., "Japan's Supersonic Technology and Business Jet Perspectives," AIAA Paper 2013–21, 2013.

[17] Morgenstern, J. M., Buonanno, M., and Nordstrud, N., "N+2 Low Boom Wind Tunnel Model Design and Validation," AIAA Paper 2012–3217, 2012.

[18] Morgenstern, J., Norstrud, N., Sokhey, J., Martens, S., and Alonso, J. J., "Advanced Concept Studies for Supersonic Commercial Transports Entering Service in the 2018 to 2020 Period," NASA CR-2013-217820, Langley Research Center, Feb. 2013. doi:2060/20130010174.

[19] Morgenstern, J., Buonanno, M., Yao, J., Murugappan, M., Paliath, U., Cheung, L., Malcevic, I., Ramakrishnan, K., Pastouchenko, N., Wood, T., Martens, S., Viars, P., Tersmette, T., Lee, J., Simmons, R., Plybon, D., Alonso, J., Palacios, F., Lukaczyk, T., and Carrier, G., "Advanced Concept Studies for Supersonic Commercial Transports Entering Service in the 2018-2020 Period Phase 2," NASA CR-2015-218719, Langley Research Center, Jul. 2015. doi:2060/20150015837.

[20] Putnam, L. E., and Capone, F. J., "Experimental Determination of Equivalent Solid Bodies to Represent Jets Exhausting into a Mach 2.20 External Stream," NASA TN D-5553, Dec. 1969. doi:2060/19700003902.

[21] Morrison, J. H., Kleb, B., and Vassberg, J. C., "Observations on CFD Verification and Validation from the AIAA Drag Prediction Workshops," AIAA Paper 2014–202, 2014.

[22] Mavriplis, D. J., Vassberg, J. C., Tinoco, E. N., Mani, M., Brodersen, O. P., Eisfeld, B., Wahls, R. A., Morrison, J. H., Zickuhr, T., Levy, D., and Murayama, M., "Grid Quality and Resolution Issues from the Drag Prediction Workshop Series," *AIAA Journal of Aircraft*, Vol. 46, No. 3, 2009, pp. 935–950. doi:10.2514/1.39201.

[23] Pirzadeh, S. Z., "Three-Dimensional Unstructured Viscous Grids by the Advancing-Layers Method," *AIAA Journal*, Vol. 34, No. 1, 1996, pp. 43–49. doi:10.2514/3.13019.

[24] Frink, N. T., Pirzadeh, S. Z., Parikh, P., Pandya, M. J., and Bhat, M. K., "The NASA Tetrahedral Unstructured Software System," *The Aeronautical Journal*, Vol. 104, No. 1040, 2000, pp. 491–499.

[25] Ratnayake, N. A., Krist, S. E., Ghaffari, F., and Ahmed, V., "Unstructured Grid Development for the Space Launch System Liftoff and Transition Lineloads Computational Analysis," AIAA Paper 2020–672, 2020.

[26] Park, M. A., Campbell, R. L., Elmiligui, A., Cliff, S. E., and Nayani, S. N., "Specialized CFD Grid Generation Methods for Near-Field Sonic Boom Prediction," AIAA Paper 2014–115, 2014.

[27] Spalart, P. R., and Allmaras, S. R., "A One-Equation Turbulence Model for Aerodynamic Flows," *La Recherche Aérospatiale*, Vol. 1, 1994, pp. 5–21.

[28] Shur, M. L., Strelets, M. K., Travin, A. K., and Spalart, P. R., "Turbulence Modeling in Rotating and Curved Channels: Assessing the Spalart-Shur Correction," *AIAA Journal*, Vol. 38, No. 5, 2000, pp. 784–702. doi:10.2514/2.1058.

[29] Spalart, P. R., "Strategies for Turbulence Modelling and Simulations," *International Journal of Heat and Fluid Flow*, Vol. 21, No. 3, 2000, pp. 252–263. doi:10.1016/S0142-727X(00)00007-2.

[30] Allmaras, S. R., Johnson, F. T., and Spalart, P. R., "Modifications and Clarifications for the Implementation of the Spalart-Allmaras Turbulence Model," *Seventh International Conference on Computational Fluid Dynamics (ICCFD7)*, 2012.

[31] Menter, F. R., "Two-Equation Eddy-Viscosity Turbulence Models for Engineering Applications," *AIAA Journal*, Vol. 32, No. 8, 1994, pp. 1598–1605.

[32] Kirz, J., and Rudnik, R., "DLR TAU Simulations for the Second AIAA Sonic Boom Prediction Workshop," *AIAA Journal of Aircraft*, Vol. 56, No. 3, 2019, pp. 912–927. doi:10.2514/1.C034819.

[33] Schwamborn, D., Gerhold, T., and Heinrich, R., "The DLR TAU-Code: Recent Applications in Research and Industry," *European Conference on Computational Fluid Dynamics ECCOMAS CFD 2006*, 2006.

[34] Cizmas, P. G. A., Gargoloff, J. I., Strganac, T. W., and Beran, P. S., "Parallel Multigrid Algorithm for Aeroelasticity Simulations," *AIAA Journal of Aircraft*, Vol. 47, No. 1, 2010, pp. 953–961. doi:10.2514/1.40201.

[35] Harten, A., "High Resolution Schemes for Hyperbolic Conservation Laws," *Journal of Computational Physics*, Vol. 49, 1983, pp. 357–393. doi:10.1016/0021-9991(83)90136-5.

[36] Roe, P. L., "Approximate Riemann Solvers, Parameter Vectors, and Difference Schemes," *Journal of Computational Physics*, Vol. 43, No. 2, 1981, pp. 357–372. doi:10.1016/0021-9991(81)90128-5.

[37] Kim, S.-s., Kim, C., Rho, O.-H., and Hong, S. K., "Cures for the Shock Instability: Development of a Shock-Stable Roe Ccheme," *Journal of Computational Physics*, Vol. 185, 2003, pp. 342–374. doi:10.1016/S0021-9991(02)00037-2.

[38] Pandya, M. J., Diskin, B., Thomas, J. L., and Frink, N. T., "Assessment of USM3D Hierarchical Adaptive Nonlinear Method Preconditioners for Three-Dimensional Cases," *AIAA Journal*, Vol. 55, No. 10, 2017, pp. 3409–3424. doi:10.2514/1.J055823.

[39] Mani, M., Cary, A. W., and Ramakrishnan, S. V., "A Structured and Hybrid-unstructured Grid Euler and Navier-Stokes Solver for General Geometry," AIAA Paper 2004–524, 2004.

[40] Michal, T., and Krakos, J., "Anisotropic Mesh Adaptation Through Edge Primitive Operations," AIAA Paper 2012–159, 2012.

[41] Michal, T., Kamenetskiy, D. S., Marcum, D., Alauzet, F., Frazza, L., and Loseille, A., "Comparing Anisotropic Error Estimates for ONERA M6 Wing RANS Simulations," AIAA Paper 2018–920, 2018.

[42] Alauzet, F., and Loseille, A., "High-Order Sonic Boom Modeling Based on Adaptive Methods," *Journal of Computational Physics*, Vol. 229, No. 3, 2010, pp. 561–593. doi:10.1016/j.jcp.2009.09.020.

[43] Biedron, R. T., Carlson, J.-R., Derlaga, J. M., Gnoffo, P. A., Hammond, D. P., Jones, W. T., Kleb, B., Lee-Rausch, E. M., Nielsen, E. J., Park, M. A., Rumsey, C. L., Thomas, J. L., Thompson, K. B., and Wood, W. A., "FUN3D Manual: 13.6," NASA TM-2019-220416, Langley Research Center, Oct. 2019.

[44] Bibb, K. L., Gnoffo, P. A., Park, M. A., and Jones, W. T., "Parallel, Gradient-Based Anisotropic Mesh Adaptation for Re-entry Vehicle Configurations," AIAA Paper 2006–3579, 2006.

[45] Park, M. A., "Three–Dimensional Turbulent RANS Adjoint–Based Error Correction," AIAA Paper 2003–3849, 2003.

[46] Venditti, D. A., and Darmofal, D. L., "Anisotropic Grid Adaptation for Functional Outputs: Application to Two-Dimensional Viscous Flows," *Journal of Computational Physics*, Vol. 187, No. 1, 2003, pp. 22–46. doi:10.1016/S0021-9991(03)00074-3.

[47] Park, M. A., and Carlson, J.-R., "Turbulent Output-Based Anisotropic Adaptation," AIAA Paper 2010–168, 2010.

[48] Aftosmis, M. J., Berger, M. J., and Adomavicius, G., "A Parallel Multilevel Method for Adaptively Refined Cartesian Grids with Embedded Boundaries," AIAA Paper 2000–808, 2000.

[49] Nemec, M., and Aftosmis, M. J., "Adjoint Error Estimation and Adaptive Refinement for Embedded-Boundary Cartesian Meshes," AIAA Paper 2007–4187, 2007.

[50] Wintzer, M., Nemec, M., and Aftosmis, M. J., "Adjoint-Based Adaptive Mesh Refinement for Sonic Boom Prediction," AIAA Paper 2008–6593, 2008.

[51] Kiris, C. C., Housman, J. A., Barad, M. F., Sozer, E., Brehm, C., and Moini-Yekta, S., "Computational Framework for Launch, Ascent, and Vehicle Aerodynamics (LAVA)," *Aerospace Science and Technology*, Vol. 55, 2016, pp. 189–219. doi:10.1016/j.ast.2016.05.008.

[52] Kim, K. H., Kim, C., and Rho, O.-H., "Methods for the Accurate Computations of Hypersonic Flows: I. AUSMPW+ Scheme," *Journal of Computational Physics*, Vol. 174, No. 1, 2001, pp. 38–80. doi:10.1006/jcph.2001.6873.

[53] Siemens PLM Software, *Fundamentals of Simcenter STAR-CCM+, Version 2020.1*, Siemens Digital Industries Software, Plano, TX 75024, USA, 2020.

[54] Chakravarthy, S., "A Unified-Grid Finite Volume Formulation for Computational Fluid Dynamics," *International Journal for Numerical Methods in Fluids*, Vol. 32, No. 1, 1999, pp. 309–323. doi:10.1002/(SICI)1097-0363(19990915)31:1<309::AID-FLD971>3.0.CO;2-M.

[55] Seguin, J., Gao, S., Habash, W. G., Isola, D., and Baruzzi, G., "A Finite Element Solver for Hypersonic Flows in Thermo-Chemical Non-Equilibrium, Part I," *International Journal of Numerical Methods in Heat and Fluid Flow*, Vol. 29, No. 7, 2018, pp. 2352–2388. doi:10.1108/HFF-09-2018-0498.

[56] ANSYS, Inc., *Product Documentation Release 2020 R1*, ANSYS, Inc., Canonsburg, PA 15317, USA, 2018.

[57] Nishikawa, H., and Liu, Y., "Third-Order Edge-Based Scheme for Unsteady Problems," AIAA Paper 2018–4166, 2018.

[58] van Leer, B., "Towards the Ultimate Conservative Difference Scheme. II. Monotonicity and Conservation Combined in a Second-Order Scheme," *Journal of Computational Physics*, Vol. 14, No. 4, 1974, pp. 361–370. doi:10.1016/0021-9991(74)90019-9.

[59] Barth, T. J., and Jespersen, D. C., "The Design and Application of Upwind Schemes on Unstructured Meshes," AIAA Paper 89–366, 1989.

[60] Park, M. A., Balan, A., Anderson, W. K., Galbraith, M. C., Caplan, P. C., Carson, H. A., Michal, T., Krakos, J. A., Kamenetskiy, D. S., Loseille, A., Alauzet, F., Frazza, L., and Barral, N., "Verification of Unstructured Grid Adaptation Components," AIAA Paper 2019–1723, 2019.

[61] Park, M. A., Kleb, B., Jones, W. T., Krakos, J. A., Michal, T., Loseille, A., Haimes, R., and Dannenhoffer, J. F., III, "Geometry Modeling for Unstructured Mesh Adaptation," AIAA Paper 2019–2946, 2019.

[62] Toro, E. F., Spruce, M., and Speares, W., "Restoration of the Contact Surface in the HLL-Riemann Solver," *Shock Waves*, Vol. 4, No. 1, 1994, pp. 25–34. doi:10.1007/BF014146292.

[63] Menier, V., Loseille, A., and Alauzet, F., "CFD Validation and Adaptivity for Viscous Flow Simulations," AIAA Paper 2014–2925, 2014.

[64] Hashimoto, A., Murakami, K., Aoyama, T., Ishiko, K., Hishida, M., Sakashita, M., and Lahur, P. R., "Toward the Fastest Unstructured CFD Code "FaSTAR"," AIAA Paper 2012–1075, 2012.

[65] Nakahashi, K., Ito, Y., and Togashi, F., "Some Challenges of Realistic Flow Simulations by Unstructured Grid CFD," *International Journal for Numerical Methods in Fluids*, Vol. 43, No. 6–7, 2003, pp. 769–783. doi:10.1002/fld.559.

[66] Venkatakrishnan, V., "Convergence to Steady State Solutions of the Euler Equations on Unstructured Grids with Limiters," *Journal of Computational Physics*, Vol. 118, No. 1, 1995, pp. 120–130.

[67] Obayashi, S., and Guruswamy, G. P., "Convergence Acceleration of a Navier-Stokes Solver for Efficient Static Aeroelastic Computations," *AIAA Journal*, Vol. 33, No. 6, 1995, pp. 1134–1141. doi:10.2514/3.12533.

[68] Takaki, R., Yamamoto, K., Yamane, T., Enomoto, S., and Mukai, J., "The Development of the UPACS CFD Environment," *High Performance Computing*, edited by A. Veidenbaum, K. Joe, H. Amano, and H. Aiso, Springer Berlin Heidelberg, Berlin, Heidelberg, 2003, pp. 307–319.

[69] Ishikawa, H., Tanaka, K., Makino, Y., and Yamamoto, K., "Sonic-Boom Prediction Using Euler CFD Codes with Structured/Unstructured Overset Method," Paper 2010-2.4.1, 27th International Congress of the Aeronautical Sciences (ICAS), 2010.

[70] Edwards, J. R., "A Low-Diffusion Flux-Splitting Scheme for Navier-Stokes Calculations," *Computers and Fluids*, Vol. 26, No. 6, 1997, pp. 635–659. doi:10.1016/S0045-7930(97)00014-5.

[71] Morgenstern, J. M., "How to Accurately Measure Low Sonic Boom or Model Surface Pressures in Supersonic Wind Tunnels," AIAA Paper 2012–3215, 2012.

[72] Morgenstern, J. M., "Distortion Correction for Low Sonic Boom Measurement in Wind Tunnels," AIAA Paper 2012–3216, 2012.

[73] Rallabhandi, S. K., "Advanced Sonic Boom Prediction Using the Augmented Burgers Equation," *AIAA Journal of Aircraft*, Vol. 48, No. 4, 2011, pp. 1245–1253. doi:10.2514/1.C031248.

[74] Rallabhandi, S. K., "Sonic Boom Adjoint Methodology and its Applications," AIAA Paper 2011–3497, 2011.

[75] *U.S. Standard Atmosphere, 1976*, U.S. Government Printing Office, 1976.

[76] American National Standards Institute, "Method for Calculation of the Absorption of Sound by the Atmosphere," ANSI S1.26-1995, Sep. 1995.

[77] Cleveland, R. O., "Propagation of Sonic Booms Through a Real, Stratified Atmosphere," Ph.D. thesis, University of Texas at Austin, May 1995. doi:2144/1443.

[78] Page, J. A., and Plotkin, K. J., "An Efficient Method for Incorporating Computational Fluid Dynamics into Sonic Boom Prediction," AIAA Paper 91–3275, 1991.

[79] Leatherwood, J. D., Sullivan, B. M., Shepherd, K. P., McCurdy, D. A., and Brown, S. A., "Summary of Recent NASA Studies of Human Response to Sonic Booms," *The Journal of the Acoustical Society of America*, Vol. 111, No. 1, 2002, pp. 586–598. doi:10.1121/1.1371767.

[80] Stevens, S. S., "Perceived Level of Noise by Mark VII and Decibels (E)," *Journal of the Acoustical Society of America*, Vol. 51, No. 2B, 1972, pp. 575–601. doi:10.1121/1.1912880.

[81] Loubeau, A., Naka, Y., Cook, B. G., Sparrow, V. W., and Morgenstern, J. M., "A New Evaluation of Noise Metrics for Sonic Booms Using Existing Data," *AIP Conference Proceedings*, Vol. 1685, No. 1, 2015, p. 090015. doi:10.1063/1.4934481.

[82] Shepherd, K. P., and Sullivan, B. M., "A Loudness Calculation Procedure Applied to Shaped Sonic Booms," NASA TP-3134, Langley Research Center, Nov. 1991. doi:2060/19920002547.

[83] Wang, J.-L., Chiou, J.-M., and Müller, H.-G., "Functional Data Analysis," *Annual Review of Statistics and Its Application*, Vol. 3, No. 1, 2016, pp. 257–295. doi:10.1146/annurev-statistics-041715-033624.

[84] "Research Opportunities in Aeronautics – 2008 (ROA-2008)," Amendment 7 to the NASA Research Announcements (NRA), Appendix A-4 NNH08ZEA001N, Mar. 2008.

[85] Kubota, H., "Sonic Boom Research in Japan," AIAA Paper 2003–3578, 2003.

[86] Phillips, B. D., and West, T. K., IV, "Multifidelity Uncertainty Quantification of a Commercial Supersonic Transport," AIAA Paper 2018–2851, 2018.